

## Intrinsic versus extrinsic effects of the grain boundary on the properties of ferroelectric nanoceramics

Yu Su,<sup>1,\*</sup> Hui Kang,<sup>1</sup> Yang Wang,<sup>2</sup> Jackie Li,<sup>3</sup> and George J. Weng<sup>2</sup>

<sup>1</sup>*Department of Mechanics, School of Aerospace Engineering, Beijing Institute of Technology, Beijing 100081, People's Republic of China*

<sup>2</sup>*Department of Mechanical and Aerospace Engineering, Rutgers University, New Brunswick, New Jersey 08903, USA*

<sup>3</sup>*Department of Mechanical Engineering, The City College of New York, New York, New York 10031, USA*

(Received 4 November 2016; published 24 February 2017)

As the grain size decreases to the nanometer range, the characteristics of the ferroelectric nanoceramic can be ultimately determined by the competition between two effects: the intrinsic effect that is associated with the local properties of the grain boundary and the extrinsic effect that arises from the dynamics of domain structure which is highly influenced by the depolarization field caused by the grain boundary. In this work we investigate such a competition with a phase-field simulation based on the time-dependent Ginzburg-Landau kinetic equation. The study is performed on poled/unpoled nanoceramics under high- and low-amplitude bipolar alternating electric field with selected grain size and loading frequency. Our calculations for poled BaTiO<sub>3</sub> at 100 Hz show that, for the grain size from 170 to 50 nm, its properties are dominated by the extrinsic effect, and from 50 to 10 nm, they are dominated by the intrinsic one. As the grain size decreases, the dielectric and piezoelectric constants at the remnant state continuously rise in the extrinsic-dominated region and then drop sharply in the intrinsic-dominated region. Our frequency calculations from 10 to 2500 Hz at the grain size of 100 nm indicate that the high-frequency behavior is very similar to that of the small grain-size, intrinsic-dominated one, whereas the low-frequency behavior is closely related to that of the large grain-size, extrinsic-dominated part, with the demarcation line occurring around 400 Hz. For the unpoled ceramics under small-signal loading, the intrinsic effect is dominant over the entire range of grain size and frequency.

DOI: [10.1103/PhysRevB.95.054121](https://doi.org/10.1103/PhysRevB.95.054121)

### I. INTRODUCTION

Ferroelectric nanoceramics share outstanding application prospects with other types of ferroelectrics in the field of microelectronics, data storage, microsensors, transducers, and actuators [1]. In addition to the complex microstructures inherited from their coarse-grained counterpart, ferroelectric nanoceramics possess some very unique features: the grain boundary area to volume ratio is much higher [2]; the non-180° domain twinning was reported being less popular [3,4]; the monodomain structure is relatively easy to form [5]; and the elastic clamping in the grains is believed to be more severe [4,6]. As a consequence, there are quite a few challenging problems in the study of ferroelectric nanoceramics. Specifically, the grain-size dependence of the dielectric, piezoelectric, and ferroelectric properties has attracted much attention in the past decade [7]. A great number of experimental studies [5,8,9] confirmed that a peak value of the dielectric/piezoelectric constant is generally formed as the grain size reduces to the submicron region. Meanwhile some key ferroelectric properties, which are characterized by the hysteresis behavior [10], such as the coercive field, remnant polarization, actuation strain, etc., are found to vary with the grain size, too [11,12]. As the advances in nanoprocessing technology further push the grain size to a lower limit [13,14], there is an immediate need to understand the grain-size-dependent properties of ferroelectric nanoceramics over the range from 200 nm down to several nanometers.

The cause of grain-size dependence in fine/ultrafine-grained ferroelectrics is multifold. Investigations were carried out

toward the understanding of such size-dependent phenomena and some key aspects—either intrinsic or extrinsic—correlated to the size dependence have been identified through the studies. Frey *et al.* [15] and Buscaglia *et al.* [16] showed that the distinct local property of the grain boundaries plays an important role in the size dependence. Frey and Payne [4] and Huan *et al.* [5] examined the variation in the density of the non-180° domain wall upon the reduction of grain size and correlated it to the intensified elastic constraint that could affect the overall properties [6,17]. More recently, Ghosh *et al.* [8] investigated the 90° domain wall dynamics in submicron-grained barium titanate (BaTiO<sub>3</sub>) ceramics and discovered that the grain-size-dependent property is mainly attributed to the variation in the domain wall mobility. They found no significant change in the residual internal stress along the reduction of the grain size.

Among the aforementioned aspects, the grain-boundary influence turns to be most significant once the grain size is very small, i.e., below 200 nm. Based on earlier studies [11] the grain-boundary influence can be divided into an intrinsic part and an extrinsic part. The intrinsic part is directly attributed to the local property of the grain boundary, which will take over the overall effective property of the material once the surface area to grain volume ratio is very high (e.g., dilution effect). The extrinsic part affects the physical property through the domain structural dynamics, which is highly influenced by the interaction between the grain boundary and the grain interior, such as the depolarization field near the grain boundary [18]. Despite the earlier research efforts, however, an emerging consensus on the specific level of significance of the role played by the intrinsic/extrinsic grain-boundary effects remains blurred. This is simply because there is yet insufficient experimental data for the grain size varying in

---

\*Corresponding author: [adamyusu@bit.edu.cn](mailto:adamyusu@bit.edu.cn)

this range. Difficulty in sample preparation, testing, and *in situ* microstructure examination is the major obstacle to conducting a consistent study on this problem. On top of that, a consistent characterization system must be implemented for the analysis. It has been demonstrated that the properties of ferroelectric ceramics are also frequency sensitive [19,20]. The applied field with varied frequencies will significantly affect the measured effective properties. In addition, different testing approaches can lead to separate observations, too. For instance, measurements performed on poled ceramics under high-strength field (above the coercive field) and on unpoled ceramics under small-signal perturbation (far lower than the coercive) can both be found in the literature [8,11,21,22]. For the investigation on poled ceramics, however, reports regarding moderate-to-high-frequency properties are seldom seen. One obvious reason is the difficulty in achieving a strong ac field with relatively high frequency in ferroelectric ceramics. It is only until very recently that a few strong-field, high-frequency tests were reported [23,24]. Some of the unique features include the continuous rise and sharp drop of coercive field and remnant polarization at high frequency. Indeed, the need to understand the strong-field frequency-dependent properties—especially under moderate-to-high frequencies—has emerged.

In view of the stated reasons, we feel that there is an urgent need to perform a consistent study of the intrinsic and extrinsic grain-boundary effects on the grain-size-dependent properties of ferroelectric nanoceramics. To this end we will carry out a phase-field simulation. It is hoped that the study could help identify the level of significance of both effects as well as the underlying mechanism for the grain-size-dependent phenomena. We will also evaluate the influence of electric-field loading frequency and testing mode (under poled or unpoled conditions) in this work. The considered material is BaTiO<sub>3</sub> nanoceramic, which is assumed to be in tetragonal state at room temperature. The considered average grain size ranges from 10 to 170 nm, and the selected electric-field frequency ranges from 10 up to 2500 Hz. In recent years, the phase-field approach was successfully employed in the study of domain patterns and structures in ferroelectric single crystals [25,26], thin films [27–29], and polycrystals [18,30]. It is a robust and versatile method for studying interfacial problems of a wide spectrum of physical phenomena, such as the flexoelectric coupling [31,32] and fracturing [33,34] in ferroelectric solids. At present, there are several different versions of the phase-field approach for ferroelectric materials in the literature [35–41]. Here we will adopt the framework established in Su and Landis [37] to carry out the analysis. The microstructure of the material is modeled with an aggregate of nanoscaled grains of predefined geometry. The electrical polarization in the grain boundary, which is located at the exterior layer of each individual grain, is assumed to be completely depressed, forming a “dead-layer” zone [15,18]. Periodic boundary conditions are employed in the model. To study the frequency influence, we take the view that the frequency dependence of ferroelectric behavior is a result of direct competition between the speed of polarization evolution and the speed of external loading [30]. The evolution of polarization is evaluated with varied levels of electric-field frequency under such framework. Underlying domain patterns will also be reported.

## II. THE PHASE-FIELD APPROACH TO THE MICROSTRUCTURAL DYNAMICS IN FERROELECTRIC CRYSTALS

In the work of Su and Landis [37], a phase-field approach was established to obtain the time-dependent multiphysical solution for the boundary-value problem of ferroelectric crystals. The temporal evolution of the electrical polarization as well as the displacement and electric potential are computed under the applied external field. In the phase-field approach, the total free energy of a system,  $F$ , is given by the volume integral of the energy density,  $\psi$ , as

$$F = \int_V \psi(P_i, P_{i,j}, \varepsilon_{ij}, D_i) dV, \quad (1)$$

where  $P_i$  is the electrical polarization vector,  $P_{i,j}$  its gradient ( $P_{i,j} = \partial P_i / \partial x_j$ ),  $\varepsilon_{ij}$  the strain tensor, and  $D_i$  the electric displacement vector. The components of the electrical polarization are taken as the order parameters of the system. The variational derivative of the free energy with respect to the polarization is given by

$$\frac{\delta F}{\delta P_i} = \frac{\partial \psi}{\partial P_i} - \frac{\partial}{\partial x_j} \left( \frac{\partial \psi}{\partial P_{i,j}} \right), \quad (2)$$

where  $\delta F / \delta P_i$  is the thermodynamic conjugate to  $\partial P_i / \partial t$ , and its negative serves as the thermodynamic driving force for the evolution of the polarization vector,  $P_i$ .

As the system evolves toward equilibrium, its total free energy continues to decrease. The evolution of  $P_i$  can be simply correlated with its driving force in a linear form, as

$$\begin{aligned} \frac{\partial P_i(x,t)}{\partial t} &= -L_{ij} \frac{\delta F}{\delta P_j(x,t)}; \quad \text{or} \quad \beta_{ij} \frac{\partial P_j}{\partial t} \\ &= \frac{\partial}{\partial x_j} \left( \frac{\partial \psi}{\partial P_{i,j}} \right) - \frac{\partial \psi}{\partial P_i}, \end{aligned} \quad (3)$$

where  $L_{ij}$  are the components of the positive-definite kinetic coefficients, and  $\beta_{ij}$  the components of the inverse mobility tensor. Equation (3) is the time-dependent Ginzburg-Landau (TDGL) kinetic equation for the evolution of the order parameter,  $P_i$ .

A general form of the Landau-Ginzburg-Devonshire energy density function [42–44] for BaTiO<sub>3</sub> can be written as [37]

$$\begin{aligned} \psi &= \frac{1}{2} a_{ijkl} P_{i,j} P_{k,l} + \left\{ \frac{1}{2} \bar{a}_{ij}(T) P_i P_j + \frac{1}{4} \bar{\bar{a}}_{ijkl} P_i P_j P_k P_l \right. \\ &\quad + \frac{1}{6} \bar{\bar{\bar{a}}}_{ijklmn} P_i P_j P_k P_l P_m P_n \\ &\quad \left. + \frac{1}{8} \bar{\bar{\bar{\bar{a}}}}_{ijklmnpqrs} P_i P_j P_k P_l P_m P_n P_r P_s \right\} \\ &\quad + \left\{ b_{ijkl} \varepsilon_{ij} P_k P_l + \frac{1}{2} c_{ijkl}^H \varepsilon_{ij} \varepsilon_{kl} + f_{ijklmn} \varepsilon_{ij} \varepsilon_{kl} P_m P_n \right. \\ &\quad \left. + g_{ijklmn} \varepsilon_{ij} P_k P_l P_m P_n \right\} + \frac{1}{2\kappa_0} (D_i - P_i)(D_i - P_i). \end{aligned} \quad (4)$$

In this function, the first term represents the gradient energy of the diffuse domain walls, which is also referred to as the exchange energy. The four terms within the first pair of braces

consist of the Landau-type energy that is used to create the nonconvex energy landscape of the free energy with minima located at the spontaneous polarization states. The four terms in the second pair are used to fit the spontaneous strain along with the dielectric, elastic, and piezoelectric properties about the spontaneous state. The final term represents the energy stored within the free space occupied by the material, where  $\kappa_0$  is the permittivity of free space. Among all the coefficients, only  $\bar{a}_{ij}$  which represent the dielectric stiffness are temperature dependent. The eighth-rank term on the  $P$  components was introduced for better adjustment of the dielectric properties and energy barrier of the  $90^\circ$  switch [45]. The sixth-rank terms represented by  $f_{ijklmn}$  and  $g_{ijklmn}$  have been introduced for better fit of elastic, piezoelectric, and dielectric properties of the low-symmetry phase in the spontaneous state. Without these two terms the elastic properties of the material arise only from the  $c_{ijkl}^H$  tensor, which has the symmetry of the high-temperature phase.

The quantities of  $D_i$  and  $\varepsilon_{ij}$  are related to  $P_i$  through the constitutive relations

$$\begin{aligned} D_i &= \kappa_0 E_i + P_i, \\ \sigma_{ij} &= c_{ijkl}(\varepsilon_{kl} - \varepsilon_{kl}^*), \end{aligned} \quad (5)$$

where the stress-free strains  $\varepsilon_{ij}^*$  depend on  $P_i$  through the polynomials

$$\varepsilon_{ij}^* = \bar{Q}_{ijkl} P_k P_l. \quad (6)$$

The electrostrictive tensor  $\bar{Q}_{ijkl}$  assures that  $\varepsilon_{ij}^*$  evolves from zero to the spontaneous strain  $\varepsilon_{ij}^{sp}$  as the polarization changes from zero to the spontaneous state,  $P_i^{sp}$ . The elastic moduli  $c_{ijkl}$  also change from the form of higher symmetry to a lower one as the electrical polarization evolves from zero to the spontaneous state. The quantities of all the considered fields, i.e., electric field, electric displacement, polarization, stress and strain, are position dependent. The physical quantities  $D_i$ ,  $\varepsilon_{ij}$ , and  $P_i$  are coupled to each other by the constitutive relations, and they are solved simultaneously, not sequentially. In our calculations, we used the quasistatic form of the Maxwell equation, the mechanical equilibrium equation, and the TDGL equation together to construct a weak form of the virtual work formula, and numerically solve them by the finite element method. A more comprehensive description of this phase-field approach and the value of the parameters in Eq. (4) can be found in the referred work [18,37,46].

The specific form of the kinetic coefficient tensor  $L_{ij}$  in our calculations is taken to be isotropic as  $L\delta_{ij}$ , where  $\delta_{ij}$  is the Kronecker delta. Although a direct measurement of  $L$  is seldom seen, its value can be indirectly determined through comparison of the overall responses obtained by this phase-field computation and available experimental observations. An appropriate value of  $L$  ( $4 \times 10^{-6} \text{ C}^2/\text{m}^2 \text{ N s}$ ) can be determined such that the numerically obtained overall frequency-dependent characteristics of the nanoceramic are comparable to some existing observations. In particular, the validity of this determined value of  $L$  will be confirmed through comparison with the experimental data of Hossain *et al.* [24], wherein their observed trends of coercive field and remnant polarization and the critical frequency are shown to

be in remarkable agreement with our numerical result [to be demonstrated in Figs. 8(a) and 8(b)].

### III. THE TWO-DIMENSIONAL COMPUTATIONAL MODEL OF $\text{BaTiO}_3$ NANOCERAMICS WITH THE DEAD-LAYER GRAIN BOUNDARY

It is computationally prohibitive to conduct a phase-field simulation in the real space range of a testing sample over numerous distributed grains, especially while considering the complex microstructure morphology near the grain boundary. In this study we devised a two-dimensional (2D) computational polycrystal model with the “dead-layer” assumption for the grain-grain interface to represent the structure of a nanocrystalline polycrystal, as shown in Fig. 1. A unit cell of the polycrystal with periodic geometry is employed. Figure 1(a) shows a portion of the overall look of the arranged grains, with one representative unit marked by the dotted-line frame. A similar scheme of idealized representation of the grain structure has also been adopted by Guo *et al.* [47] and Ma *et al.* [48]. The grain structure is determined with respect to a

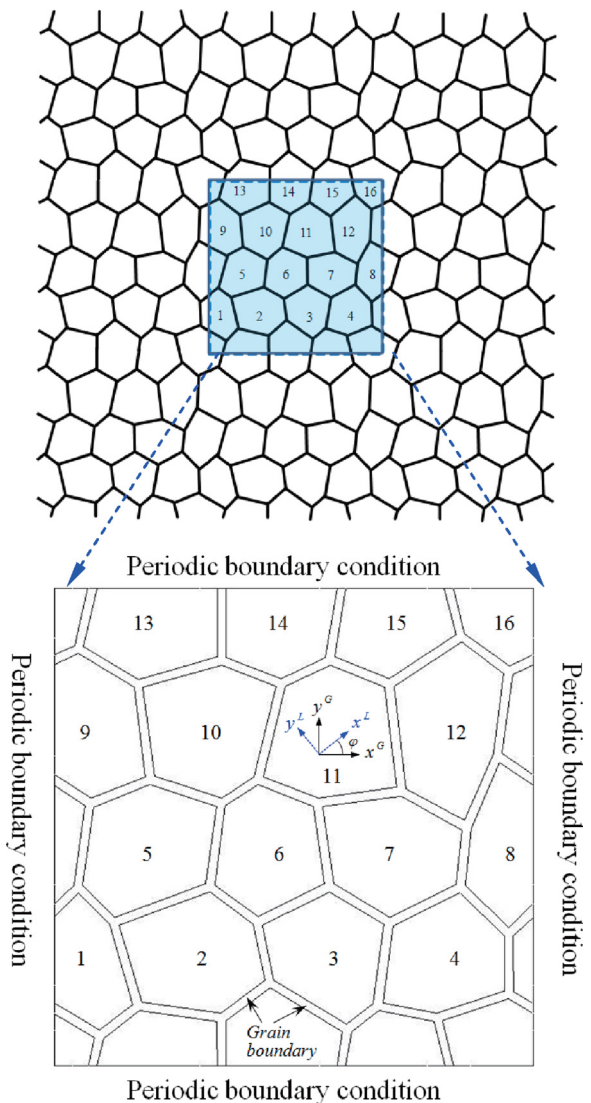


FIG. 1. The schematic of the polycrystalline model.

scanned topography image of a dense nanocrystalline BaTiO<sub>3</sub> ceramic, and the grains in the model are made in comparable size to each other. Figure 1(b) illustrates the unit cell with the grain-grain interface featured by the dead layer. The dead layer is assumed to be amorphous without spontaneous polarization. Thus the material in the dead layer is effectively paraelectric with lower dielectric permittivity than the grain interior. Such dead-layer model is different from the core-shell model which has been previously established by Su *et al.* [30]. In the core-shell model, the material near the grain boundary stays in a weak ferroelectric state with both lower dielectric constant and lower spontaneous polarization compared to the grain interior. The reason to select the dead-layer model relies on the fact that there exist quite a number of microstructural observations [13,15,16,49,50] of ferroelectric nanoceramics showing supportive evidence to such assumption.

All the computations are under the assumption of a plane problem. The out-of-plane components of the polarization, electric field, and electric displacement are zero, i.e.,  $P_3 = 0$ ,  $E_3 = 0$ , and  $D_3 = 0$ . Generalized plane strain is assumed for the mechanical fields, i.e.,  $\varepsilon_{13} = \varepsilon_{23} = 0$ ,  $\varepsilon_{33} = -0.3259\varepsilon_0$ , and  $\sigma_{13} = \sigma_{23} = 0$ , where constant  $\varepsilon_0$  is the spontaneous strain along the  $c$  axis of BaTiO<sub>3</sub> crystal. Periodicity boundary conditions of the electric potential and the polarization vector are imposed to the boundaries of the representative unit as shown in Fig. 1(b). On the lower and upper horizontal boundaries, the periodicity conditions are given by  $\varphi(x,0) = \varphi(x,h) + Eh$  and  $P_i(x,0) = P_i(x,h)$  ( $i = 1,2$ ) for the electric potential and polarization, respectively. The constant  $h$  is the height of the representative unit cell. On the left and right vertical boundaries, the periodicity conditions are given by  $\varphi(0,y) = \varphi(w,y)$  and  $P_i(0,y) = P_i(w,y)$  ( $i = 1,2$ ), where the constant  $w$  is the width of the representative unit cell. The equilibrium of surface charge and surface gradient flux at the boundaries were ensured via the method of multipoint constraints during the finite element procedure.

The representative unit consists of 16 typical grains with local crystal lattice orientations varying gradually from 0° to 90°. These angles are randomly assigned to these 16 grains. The computation procedure starts with an initial condition wherein the polarization is randomly aligned along the local crystal lattice of each grain. A sufficient time period is taken to allow for full relaxation and then followed by increments of uniaxially applied electric field. In order to represent the microstructure of the nanoceramic, the choice of the polycrystal grain assembly must possess sufficient isotropy. With grain orientations varying uniformly from 0° to 90° and with the angles randomly assigned to these 16 grains, our choice of grain assembly possesses sufficient in-plane isotropy based on the lamination theory. The further increase of grain number or orientation angle would not deliver fundamentally different physical characteristics. In our calculations we have set the dielectric permittivity of the dead layer to be 35% of the grain interior. Such properties were set through adjustment of its Landau coefficients in Eq. (4). We took the thickness of the dead layer to be 0.8 nm [15], regardless of the grain size. During the numerical analysis, the transition conditions between the grains through the dead layer are controlled through the compatibility of the strain field, electric displacement, and polarization. These transitions are

fulfilled continuously, from one field point to another, from one grain to the dead layer, and then to the neighboring grain.

The frequency dependence of the BaTiO<sub>3</sub> nanoceramics was studied by applying a uniaxial electric field to the developed model in Fig. 1(b). A time-dependent sinusoidal electric field can be achieved through the setting of electric potentials in the boundary conditions, with

$$E = E_{\max} \sin(2\pi ft), \quad (7)$$

where  $E_{\max}$  is the amplitude of the applied field and  $f$  the loading frequency. During the study of the frequency dependence under a high-amplitude field, the value of  $E_{\max}$  is set to be sufficiently high to ensure the saturation of polarization switching. Here the value of  $E_{\max}$  is set to  $E_0$ , the field needed to completely switch a uniform domain of BaTiO<sub>3</sub> crystallite. In the case of small-signal computation, the value of  $E_{\max}$  is set as 1% $E_0$ . The mechanical boundary condition is set to be traction-free. In all cases the local stress field stemming from the piezoelectric effect is fully considered in our calculations. All the obtained results are meant to be read according to the current boundary-condition configuration as described in this section.

#### IV. RESULTS AND DISCUSSION

Based on the aforementioned polycrystalline model, we have carried out the phase-field analysis with an induced bipolar ac electric field as described in Eq. (7). For each computation, a constant frequency was set within the range from 10 to 2500 Hz. The average grain size of the polycrystal model was selected from 170 down to 10 nm. For the simulation on both the poled and unpoled ceramics, it started with zero applied electric field, such that the electrical polarization in the material is in a completely relaxed state. After that, the electric field in a sinusoidal form was applied. For the simulation on poled ceramics, a stable hysteresis loop (electric displacement vs electric field) and a butterfly loop (the axial strain vs electric field) can be obtained after several cycles of loading/unloading. Based on the numerical results, we now report the intrinsic and extrinsic effects of the grain boundary on the ferroelectric properties of BaTiO<sub>3</sub> nanoceramics.

##### A. Transition from the extrinsic-dominated to the intrinsic-dominated effect as grain size decreases

###### 1. High-amplitude loading on poled nanoceramics

Under the high-amplitude bipolar ac field at a constant frequency of 100 Hz, the hysteresis loop and the butterfly loop of the poled nanoceramics were obtained with the average grain size being 10, 20, 40, 50, 80, 100, 130, and 170 nm, respectively. Figures 2(a) and 2(b) show the obtained results with remarkable grain-size dependence. The hysteresis loop, as illustrated in Fig. 2(a), becomes more tilted as the average grain size becomes smaller. Meanwhile, both the remnant polarization and the coercive field also decrease. Specifically, the hysteresis loop becomes severely tilted and the behavior approaches a superparaelectric characteristic once the grain size is below 20 nm. Such characteristic highly agrees with experimental observations of BaTiO<sub>3</sub>-based nanoceramics [2,15,16,51,52]. The nonlinear electromechanical coupling

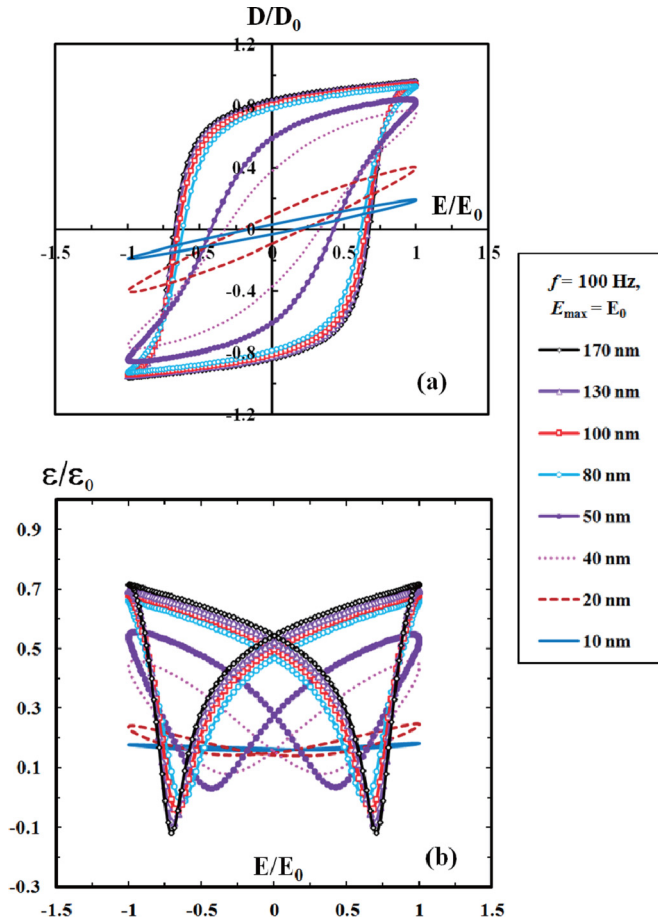


FIG. 2. The computed grain-size dependence of (a) the hysteresis loop and (b) the butterfly loop of the poled nanoceramics with varied grain size.

behavior, as shown in Fig. 2(b), also evolves from a typical butterfly shape to a flattened one as the grain size reduces. In particular, the “tails” of the butterfly loop disappear when the grain size is smaller than 20 nm, confirming the freeze of polarization switching in the material. The actuation strain (the maximum difference in the axial strain under the applied electric field) becomes nearly negligible for the case of very small grain size.

Based on these results, the values of the remnant polarization, coercive field, and axial actuation strain are plotted in Fig. 3 as the average grain size decreases from 170 down to 10 nm. The reference electric displacement, electric field, and strain are set at  $D_0 = 0.26 \text{ C/m}^2$ ,  $E_0 = 218 \text{ kV/cm}$ , and  $\epsilon_0 = 0.82\%$ ; these correspond to the known values of spontaneous polarization, the field needed to completely switch a uniform domain, and axial spontaneous strain in BaTiO<sub>3</sub> crystal [37]. As shown in the plot, all three quantities decrease monotonically as the grain size reduces. During this process, the reduction of the quantities is relatively slow from 170 to 50 nm, and becomes very drastic from 50 down to 10 nm, which we mark in blue. Such monotonic decrease of remnant polarization and coercive field agrees with the observations by Mudinepalli *et al.* [21] on poled BaTiO<sub>3</sub>-based nanoceramics. The transition in Fig. 3 is seen to occur around the grain size of 50 nm.

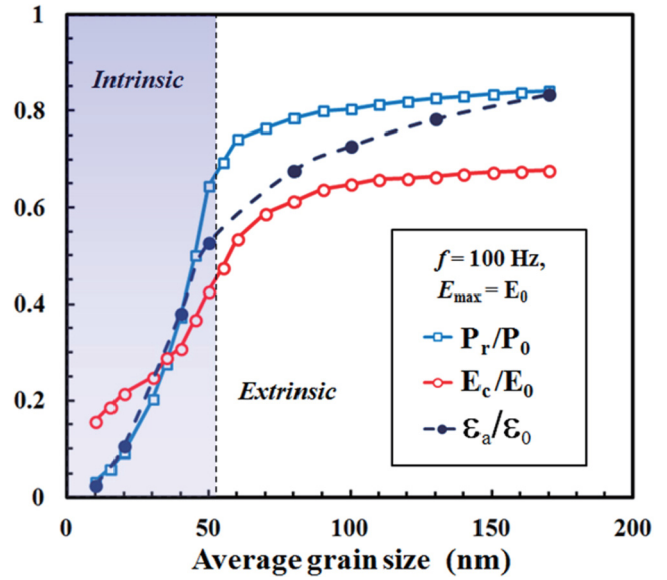


FIG. 3. The grain-size dependence of remnant polarization, coercive field, and actuation strain of the poled nanoceramics.

The differential dielectric coefficient at the remnant state ( $\kappa_r$ ) and the coercive state ( $\kappa_c$ ), as well as the differential piezoelectric coefficient at the remnant state ( $d_{33}$ ), are found to be varying with the average grain size, too. In Fig. 4, the values of  $\kappa_r/\kappa^0$ ,  $\kappa_c/\kappa^0$ , and  $d_{33}/d^0$  are plotted as functions of the average grain size. The reference permittivity  $\kappa^0$  and the reference piezoelectric constant  $d^0$  are set being equal to  $D_0/E_0$  and  $\epsilon_0/E_0$ , respectively. It is noticed that, as the grain size decreases, the values of  $\kappa_r$  and  $d_{33}$  both increase from 170 down to 50 nm, and then quickly drop from 50 down to 10 nm. The peaks form at 50 nm. There is also a change of curvature in the  $\kappa_c$  curve at 50 nm. We also note that the increase part of the remnant dielectric

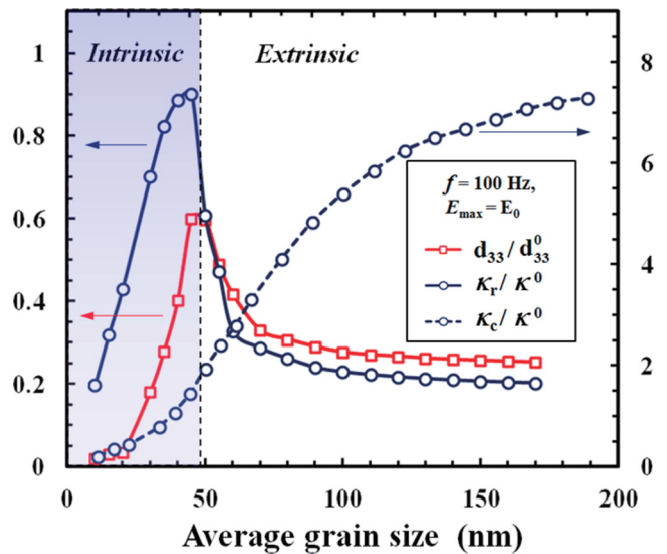


FIG. 4. The grain-size dependence of the differential dielectric constant at the remnant state and coercive state, and the remnant piezoelectric constant for poled nanoceramics.

constant is also consistent with the observation of Mudinepalli *et al.* [21] which reported the change from 200 nm down to 60 nm.

The strong-field properties reported in Figs. 3 and 4 clearly point to the separation of the small grain-size region marked in blue from the large grain-size region marked in white. They are separated at 50 nm. In the blue region, the local property of the grain boundary is dominant, so this region is dominated by the intrinsic effect. As a consequence the effective dielectric permittivity, piezoelectric coefficient, remnant polarization, and coercive field all decrease as the grain size decreases. In the white region, the intrinsic effect is negligible, so it is dominated by the extrinsic effect.

In general the influence of grain boundary becomes insignificant for the grain size above several microns, but its effect is significant when the grain size is in the nanoscale [2]. Apparently the grain-size dependence is a result of the combined contributions from both types of effect, and each plays a role of different level of significance at varied grain sizes. With the reduction of grain size from 170 to 10 nm, both types of effect tend to lower the remnant polarization and coercive field. But their effects on the differential dielectric and piezoelectric coefficients are competitive, leading to the rise and fall of these two quantities.

### 2. Small-signal simulation on unpoled nanoceramics

In addition to the high-amplitude hysteresis computation, we also conducted small-signal simulation on unpoled nanoceramics to examine the grain-size effect on the remnant dielectric coefficient. The motivation of this investigation lies on the fact that, in many measurements, the dielectric constant is obtained by applying a low-amplitude ac field to unpoled ferroelectrics, so it is enlightening to see the grain-size effect on the dielectric coefficient computed under small-signal perturbation. A low-amplitude ( $1\% E_0$ ) alternating bipolar electric field was then applied in the simulation to examine the remnant dielectric coefficient,  $\kappa$ , with the frequency being 100 Hz. The value of the normalized dielectric constant is plotted in Fig. 5 as a function of the average grain size, which reduces from 170 to 10 nm. It is noted that the value of the dielectric coefficient quickly drops as the grain size decreases. This result is consistent in trend with most experimental observations on unpoled nanoceramics [6,15,53].

### 3. The underlying domain patterns for poled nanoceramics

The low-permittivity paraelectric nature of the dead layer can result in a significant depolarization field near the grain-boundary interface. To compensate the strong depolarization field, the spatial distribution of the electrical polarization vectors has to disperse near the grain-boundary interface and also satisfies the continuity condition throughout the entire polycrystal. As a consequence the polarization microstructure tends to change from the single-domain to the toroidal structure as grain size decreases [18,54]. Such change also translates into the different ferroelectric characteristics for both types of grain size. To demonstrate the effect of depolarization field, we computed the distribution of the electrical polarization with the average grain size being 15 and 110 nm. The corresponding polarization distributions at the remnant state

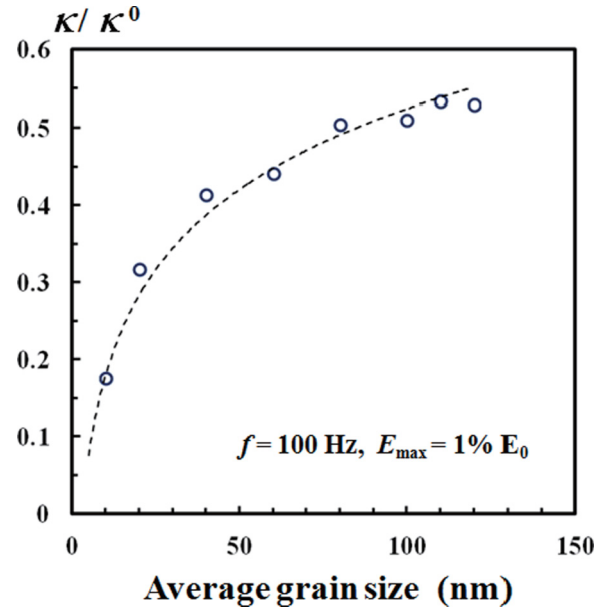


FIG. 5. The grain-size dependence of the remnant dielectric constant for unpoled nanoceramics.

are plotted in Figs. 6(a) and 6(b), respectively. It is seen that the distribution of polarization exhibits single-domain structures at 110 nm, whereas it is of the vortex nature at 15 nm when the depolarization field is particularly strong. As single-domain structures possess lower polarization switching mobility than a multidomain or a vortex structure, the coercive field with larger grain size is higher over the entire range of grain size. The higher domain mobility that comes with the decrease of grain size also implies a larger change of slope in the  $D$  vs  $E$  plot at the remnant state, and thus a higher dielectric constant. Thus, in the large grain size part (above 50 nm), decreasing the grain size will result in an increase of dielectric constant. For the same reason, it also leads to an increase of the piezoelectric constant. But below this critical grain size, the low permittivity of the dead layer eventually brings down these constants and leads to the drastic drop of their magnitudes.

### B. Transition from the extrinsic-dominated to the intrinsic-dominated effect as loading frequency increases

To examine the transition between the extrinsic and intrinsic effects as loading frequency changes, a bipolar alternating electric field was applied to the nanoceramic based on Eq. (7) with selected frequency from 10 to 2500 Hz. A common average grain size of 100 nm is set for each computation. The amplitude of the field is  $E_0$  for the high-amplitude computation and  $1\% E_0$  for the small-signal case. The obtained hysteresis and butterfly loops for poled nanoceramics are respectively plotted in Figs. 7(a) and 7(b). It is evident that the response exhibits conventional hysteresis and butterfly shapes while the frequency is relatively low. Once the frequency is increased to about 400 Hz, the hysteresis and butterfly loops start to change, eventually to a kidney shape and an ellipse shape, respectively, at 1000 Hz. Such kind of frequency-induced change was also reported by Rao *et al.* [55] on magnetic hysteresis and by Su *et al.* [30] on ferroelectric hysteresis, but

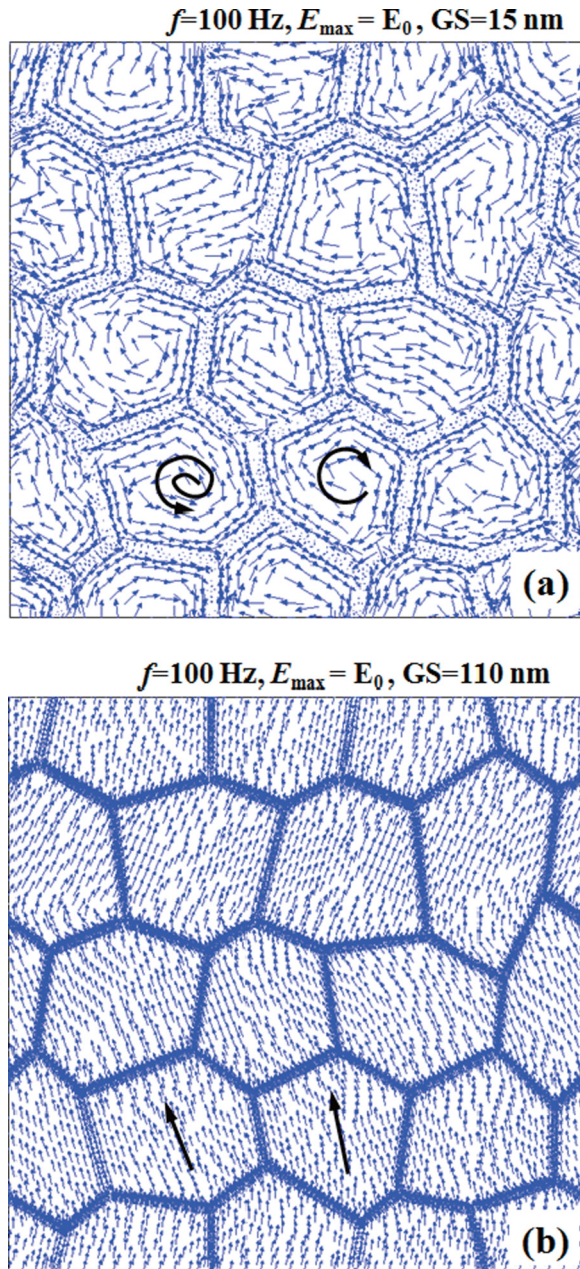


FIG. 6. The remnant-state polarization distribution of poled BaTiO<sub>3</sub> nanoceramic with the grain size of (a) 15 nm and (b) 110 nm.

here it is investigated through the polycrystalline phase-field model with the dead-layer grain boundary. In particular, as the frequency goes beyond 1000 Hz, both the hysteresis and butterfly loops show the trend of very unconventional characteristics.

The frequency dependence of the remnant polarization and coercive field is plotted in Fig. 8(a). The remnant polarization exhibits a rise followed by an immediate reduction as the frequency is increased from 10 to 2500 Hz. The coercive field exhibits an even sharper increase until about 400 Hz, then followed by a drop, all the way to 2500 Hz. Such an increase-and-then-decrease trend was very recently observed experimentally by Hossain *et al.* [24] in nanocrystalline

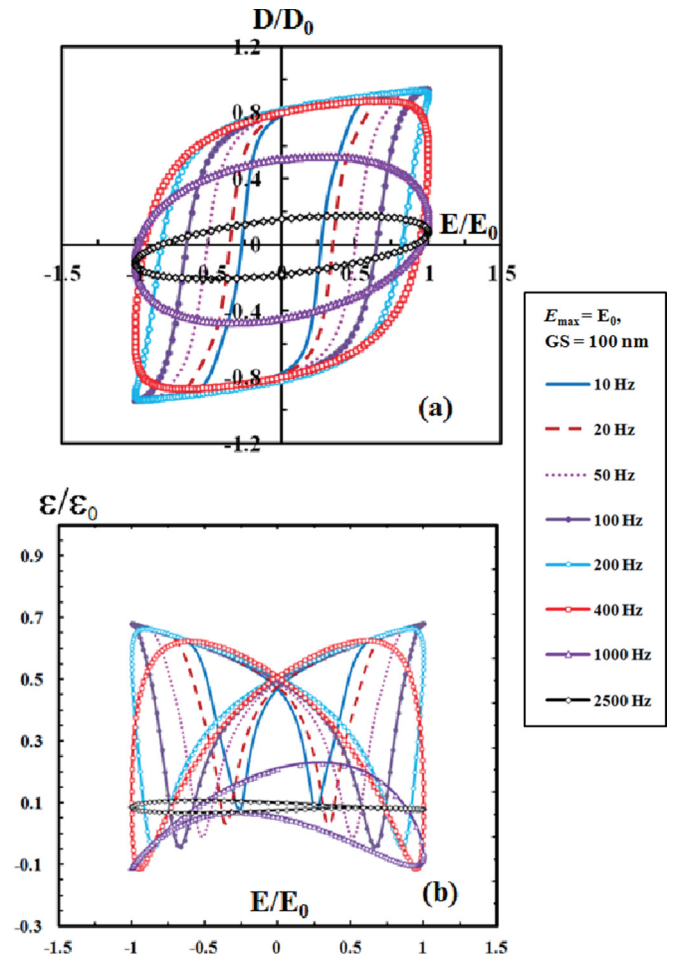


FIG. 7. The computed frequency dependence of (a) the hysteresis loop and (b) the butterfly loop.

BaMn<sub>3</sub>Ti<sub>4</sub>O<sub>14.25</sub> (BMT) polycrystals. They observed the same kind of evolution of the remnant polarization and the coercive field as the frequency of the applied field increases from 5 to 5000 Hz. In their study, the value of the remnant polarization and the coercive field of the nanocrystalline material was observed to increase with the frequency in low-frequency range (5–500Hz) and then decrease in the high-frequency range (500–5000Hz), as demonstrated in Fig. 8(b). Both Fig. 8(a) and Fig. 8(b) exhibit the transition of the properties around the same 500 Hz. This was the basis of our choice of the kinetic coefficient,  $L = 4 \times 10^{-6} \text{ C}^2/\text{m}^2 \text{ N s}$ . In addition, the frequency dependence of the differential dielectric coefficient at the remnant and the coercive states as well as the differential piezoelectric coefficient at the remnant state is plotted in Fig. 9. It is found that these three quantities all decrease with the applied frequency.

The underlying mechanism of the observed frequency-dependent characteristics lies on the direct competition between the speed of the applied electric field and the speed of the polarization switching process. The evolution of the electrical polarization in the phase-field model is time dependent. Upon the change of the applied field, each electric dipole needs a certain time to respond and another time to finalize the switching [20]. Such time-dependent process is controlled

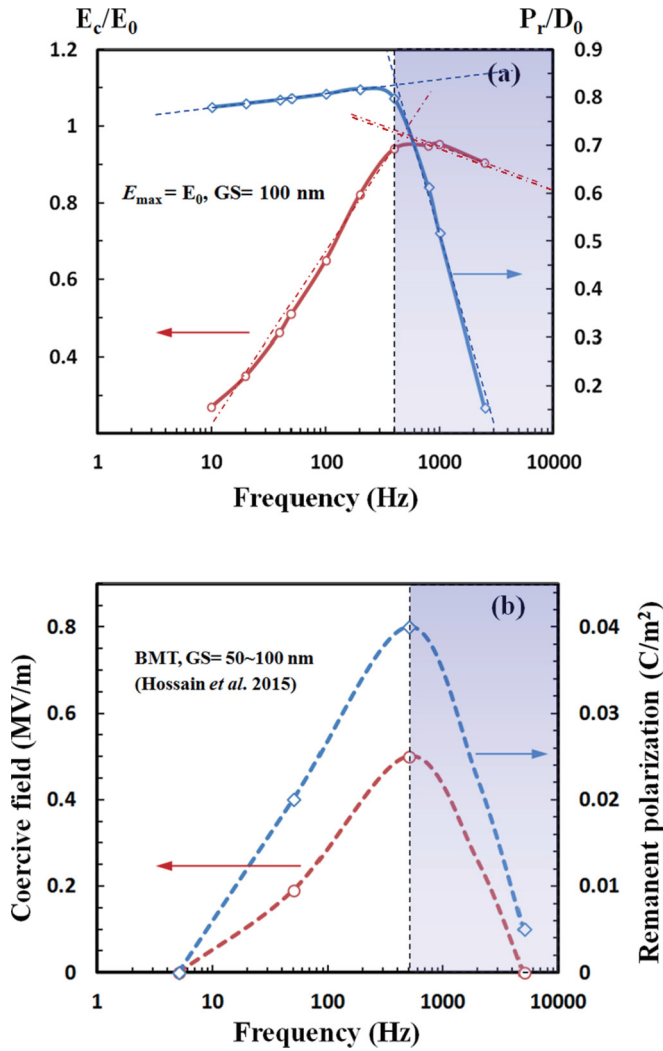


FIG. 8. The frequency dependence of the coercive field and remnant polarization for poled nanoceramics

by the Ginzburg-Landau kinetic equation [Eq. (3)] in the phase-field model. In the low-frequency range (10–400Hz) the microstructural evolution follows closely with the variation of the applied electric field. It has sufficient time to evolve toward the equilibrium state. As such, a complete 180° polar reorientation can be realized during a complete cycling. Within this frequency range, as the speed of field variation increases, the back switching of the electric dipoles starts to fall behind. As a result, the value of the remnant polarization at zero field remains mostly at the fully polarized state and thus is higher at a higher frequency. For the same reason, plus the increased resistance to polar reorientation with frequency, the coercive field also increases with the frequency. Once the frequency of the applied field is raised to a higher level (400–2500Hz), the development of polar reorientation severely falls behind and the electric dipole cannot fully rotate to the 180° direction. The outcome of the  $D$  vs  $E$  loop exhibits a trend of an ellipse. At this stage, higher applied frequency will lead to a less polarized state. As a result, the hysteresis behavior is approaching a linear dielectric behavior. Both the remnant polarization and the coercive field start to drop with the frequency. Meanwhile, a

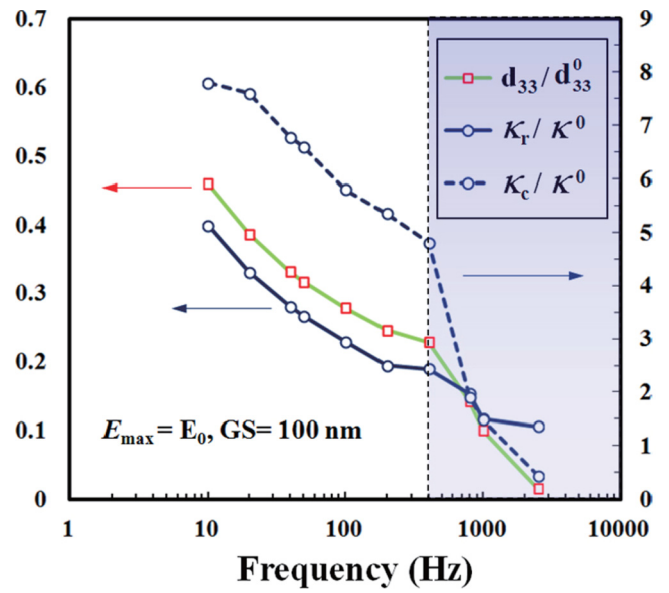


FIG. 9. The frequency dependence of the differential dielectric constant at the remnant state and coercive state, and the remnant piezoelectric constant for poled nanoceramics.

higher loading speed will leave less time for the electric dipole to respond, thus leading to a lower changing rate in the electric displacement with respect to the applied field at the remnant state. As a result, the value of the differential dielectric and piezoelectric coefficients decrease with the frequency over the entire frequency range, as shown in Fig. 9.

In both Figs. 8 and 9, we have purposefully marked the high-frequency range above 400 Hz in blue [500 Hz for BMT in Fig. 8(b)], and the low-frequency range below it in white. In the blue regions, the remnant polarization, coercive field, and the three constants,  $d_{33}$ ,  $\kappa_r$ , and  $\kappa_c$ , all continue to decrease with increasing frequency. Such a decreasing trend for all five quantities is the trademark of the blue regions in Figs. 3 and 4 that has been identified as the intrinsic-dominated

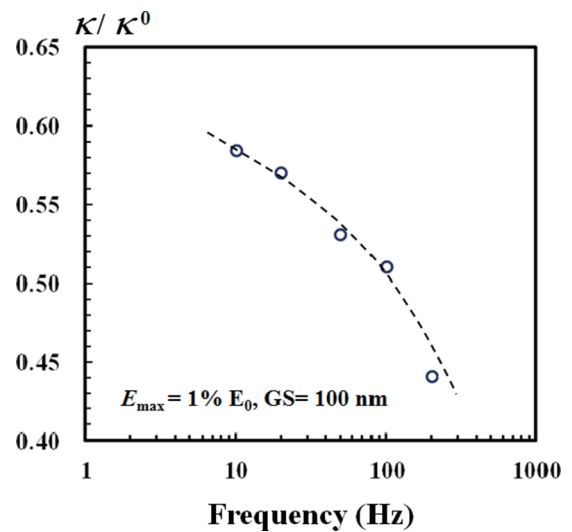


FIG. 10. The frequency dependence of the remnant dielectric constant of the unpoled BaTiO<sub>3</sub> nanoceramic.

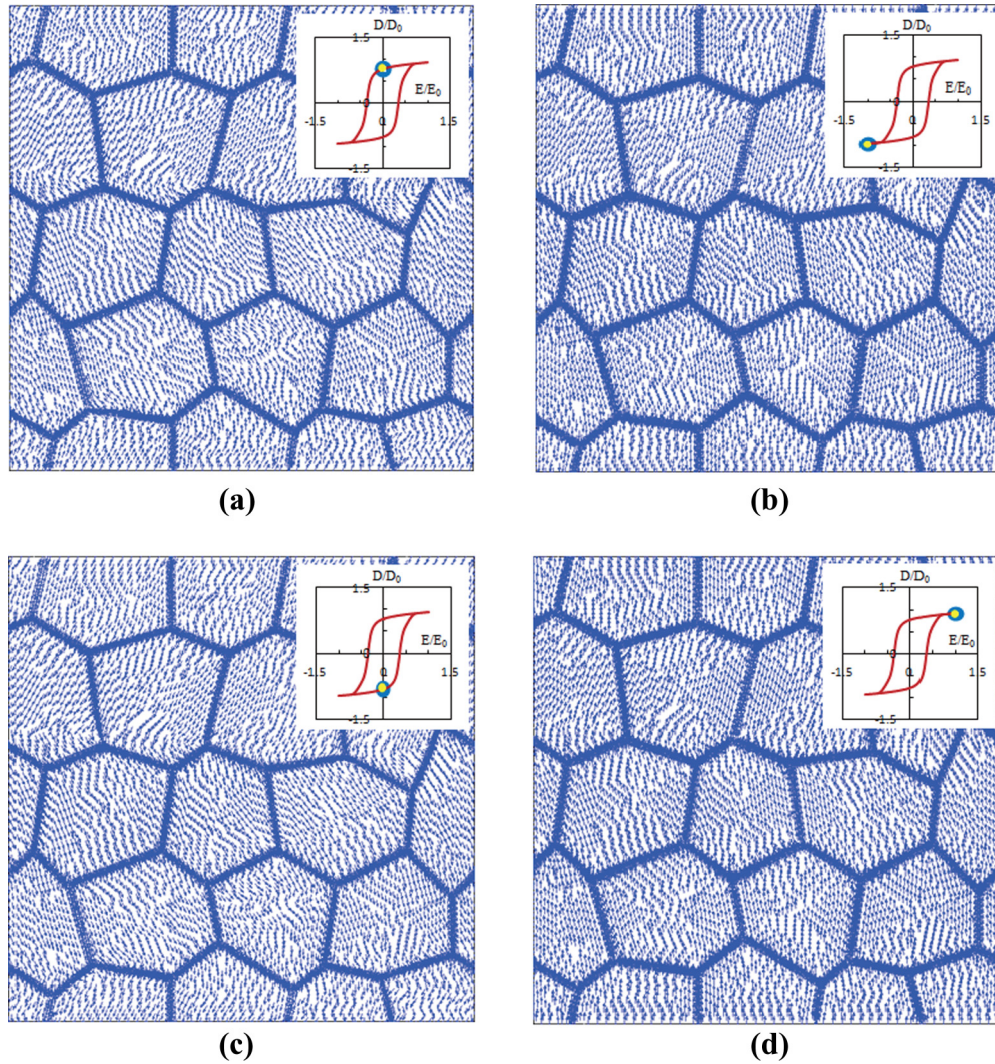


FIG. 11. The remnant-state polarization distribution of poled BaTiO<sub>3</sub> nanoceramic with the low frequency of 10 Hz with 100 nm grain size.

effects. So the effect of increasing the loading frequency at the high-frequency end is similar to the decrease of grain size at the low grain size end. In the white regions, we see that, with increasing frequency, both  $P_r$  and  $E_c$  increase, and both  $d_{33}$  and  $\kappa_r$  decrease with it. Such a trend is similar to the changes in the white regions of Figs. 3 and 4 with increasing grain size. These parallel trends allow us to draw the conclusion that the high-frequency behaviors above the critical 400 Hz exhibit the intrinsic-dominated characteristic, with increasing the loading frequency having the effect of decreasing the grain size. The low-frequency behavior below it exhibits the extrinsic-dominated mode, with increasing frequency having the same effect as increasing the grain size.

With respect to the low-amplitude simulation for unpoled nanoceramic, as the strength of the applied field is far less than the coercive field, large polar reorientation is not likely to occur during such process. However, the differential remnant dielectric coefficient, as shown in Fig. 10, is still highly dependent on the field frequency and decreases with it. In comparison with Fig. 5, we observe that increasing the

loading frequency has a similar effect as decreasing the grain size.

The reported hysteresis and butterfly loops in Figs. 7(a) and 7(b) are closely related to the underlying domain patterns. At the low frequency of 10 Hz, the variations of polarization vectors at four selected states are shown in Figs. 11(a)–11(d), and those at the high frequency of 1000 Hz are depicted in Figs. 12(a)–12(d). The former one is representative of all the low-frequency characteristics up to 400 Hz, with full polarization switch from 0 to 180°. The latter one represents those high-frequency characteristics whose polarization switch tends to stop at 90° because the speed of polar reorientation cannot catch up with the speed of external loading. One could see that the polarization vectors in Fig. 11(a) are mostly pointing up, whereas those in Fig. 11(c) are mostly pointing down, with Fig. 11(d) bringing them back to the original state. These result in the full hysteresis and butterfly loops in Figs. 7(a) and 7(b). But those in Figs. 12(a) and 12(b) do not exhibit the complete 180° switch. As a consequence the  $D$  vs  $E$  hysteresis and the  $\epsilon$  vs  $E$  butterfly loops turn into the unusual elliptic and kidney shapes, respectively.

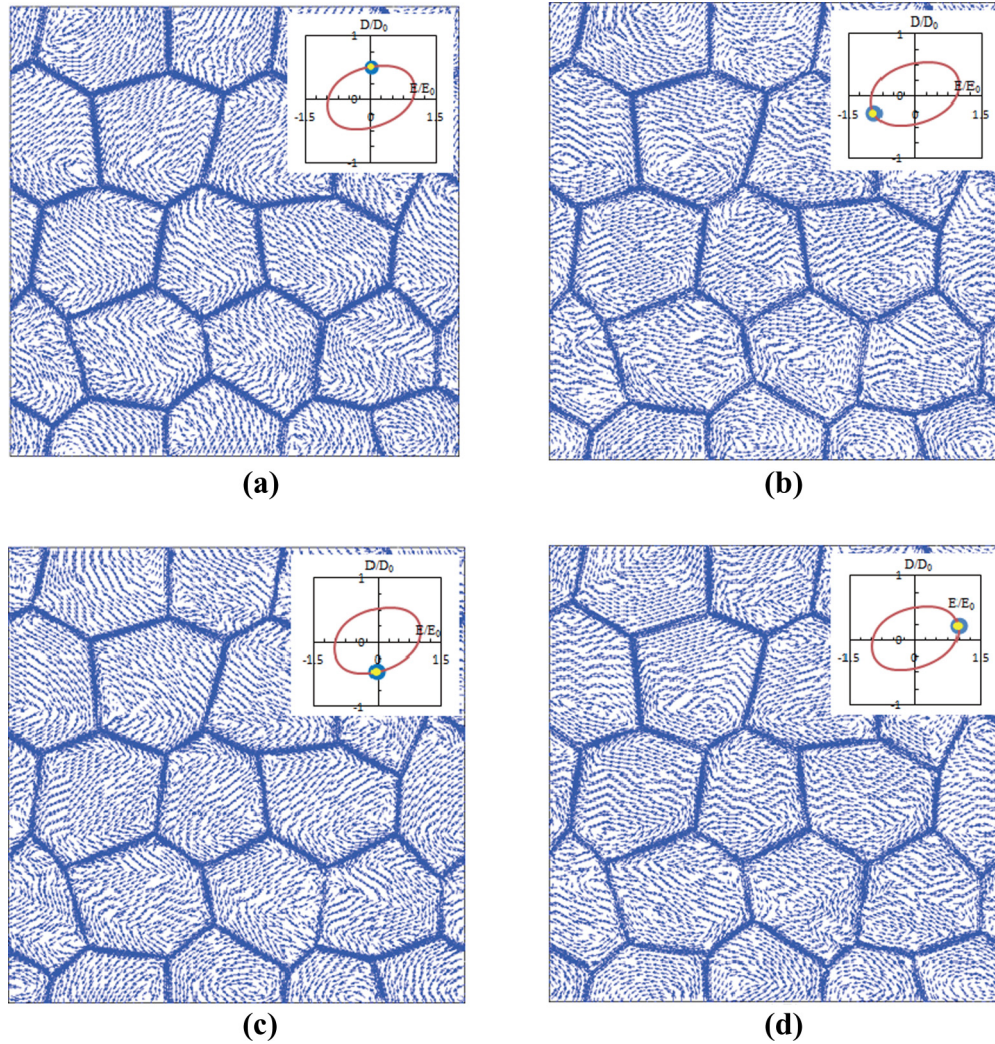


FIG. 12. The remnant-state polarization distribution of poled  $\text{BaTiO}_3$  nanoceramic with the high frequency of 1000 Hz with 100 nm grain size.

## V. CONCLUSIONS

In this phase-field study, we numerically investigated the intrinsic and extrinsic effects of grain boundary on the physical properties of  $\text{BaTiO}_3$  nanoceramics along the reduction of the grain size from 170 down to 10 nm. It was found that the low-permittivity paraelectric grain boundary possesses profound influence on the properties of the material. Under high fields as the grain size decreases, the two types of grain-boundary influence (the intrinsic and extrinsic effects) play the roles of different level of significance. The extrinsic grain-boundary effect is found to dominate the process at the high grain size range above 50 nm, and the intrinsic grain-boundary effect quickly takes over once the grain size is reduced below it. As a result, the values of the remnant dielectric and piezoelectric coefficients first increase, then rapidly decrease during the reduction of the grain size, forming a peak near the grain size of 50 nm. For the same reason, the calculated remnant polarization, coercive field, and actuation strain decrease slowly while above 50 nm and then drop quickly as the grain size is further reduced. For the small-signal computation, however, the extrinsic grain-boundary

influence is negligible since the polarization switching does not occur under such weak-field perturbation. The intrinsic grain-boundary influence dominates the entire process and leads to a monotonic decrease in the value of the dielectric coefficient.

With respect to the frequency dependence under high-amplitude field, the numerical results show that the conventional hysteresis and butterfly loops evolve to a kidney-shaped loop and an ellipse-shaped loop, respectively, as the applied frequency increases from 10 to 2500 Hz. Such an evolution is a result of the direct competition between the speed of the applied electric field and the speed of the polarization switching process. The entire process can be split into two parts: the low-frequency part wherein a complete  $180^\circ$  polar reorientation can be realized, and the high-frequency part wherein the material cannot be fully poled and a complete  $180^\circ$  reversal is absent. The obtained rise-then-drop trend of the remnant polarization and the coercive field is attributed to such microstructural mechanism, and this trend was confirmed by experimental observation on nanocrystalline  $\text{BaMn}_3\text{Ti}_4\text{O}_{14.25}$  polycrystal. This further substantiated our choice of the  $L$  value in the kinetic equation. Finally, a higher loading speed will

leave less time for the electric dipole to respond, thus leading to a lower rate of change in the electric displacement with respect to the applied field at the remnant state. It results in the decrease in both the differential piezoelectric and dielectric coefficients for poled nanoceramic as well as the decrease in the dielectric constant observed in the low-amplitude simulation.

The transition from the extrinsic-dominated effect at large grain sizes to the intrinsic-dominated mode at small grain sizes is found to be very similar to the transition from the low-frequency to the high-frequency loading. In the extrinsic range, increasing the loading frequency has the same effect as increasing the grain size. In the intrinsic range, increasing the frequency has the same effect as decreasing the

grain size. The transition from the extrinsic to the intrinsic-dominated mode was found to occur at 50 nm and 400 Hz, respectively.

#### ACKNOWLEDGMENTS

Y.S. and H.K. acknowledge the support of National Natural Science Foundation of China (Grants No. 11472045, No. 11521062, and No. 11672036). G.J.W. acknowledges the support of National Science Foundation, Mechanics of Materials Program, under Grant No. CMMI-1162431. J.L. acknowledges the support of National Science Foundation CMMI Division under Grant No. IDR-1014777.

- 
- [1] N. Setter and R. Waser, *Acta Mater.* **48**, 151 (2000).
- [2] F. Maglia, I. G. Tredici, and U. Anselmi-Tamburini, *J. Eur. Ceram. Soc.* **33**, 1045 (2013).
- [3] G. Arlt, *J. Mater. Sci.* **25**, 2655 (1990).
- [4] M. H. Frey and D. A. Payne, *Phys. Rev. B* **54**, 3158 (1996).
- [5] Y. Huan, X. Wang, J. Fang, and L. Li, *J. Am. Ceram. Soc.* **96**, 3369 (2013).
- [6] A. G. Zembilgotov, N. A. Pertsev, and R. Waser, *J. Appl. Phys.* **97**, 114315 (2005).
- [7] H. Ghayour and M. Abdollahi, *Powder Technol.* **292**, 84 (2016).
- [8] D. Ghosh, A. Sakata, J. Carter, P. A. Thomas, H. Han, J. C. Nino, and J. L. Jones, *Adv. Funct. Mater.* **24**, 885 (2014).
- [9] Y. Tan, J. Zhang, Y. Wu, C. Wang, V. Koval, B. Shi, H. Ye, R. McKinnon, G. Viola, and H. Yan, *Sci. Rep.* **5**, 9953 (2015).
- [10] L. Jin, F. Li, and S. Zhang, *J. Am. Ceram. Soc.* **97**, 1 (2014).
- [11] C. A. Randall, N. Kim, J. P. Kucera, W. Cao, and T. R. Shrout, *J. Am. Ceram. Soc.* **81**, 677 (1998).
- [12] T. Takeuchi, C. Capiglia, N. Balakrishnan, Y. Takeda, and H. Kageyama, *J. Mater. Res.* **17**, 575 (2002).
- [13] X. Wang, X. Deng, H. Wen, and L. Li, *Appl. Phys. Lett.* **89**, 162902 (2006).
- [14] X. H. Wang, I. W. Chen, X. Y. Deng, Y. D. Wang, and L. T. Li, *J. Adv. Ceram.* **4**, 1 (2015).
- [15] M. H. Frey, Z. Xu, P. Han, and D. A. Payne, *Ferroelectrics* **206**, 337 (1998).
- [16] M. T. Buscaglia, M. Viviani, V. Buscaglia, L. Mitoseriu, A. Testino, P. Nanni, Z. Zhao, M. Nygren, C. Harnagea, D. Piazza, and C. Galassi, *Phys. Rev. B* **73**, 064114 (2006).
- [17] W. R. Buessem, L. E. Cross, and A. K. Goswami, *J. Am. Ceram. Soc.* **49**, 36 (1966).
- [18] N. Liu, Y. Su, and G. J. Weng, *J. Appl. Phys.* **113**, 204106 (2013).
- [19] X. Chen, X. Dong, F. Cao, J. Wang, and G. Wang, *J. Am. Ceram. Soc.* **97**, 213 (2014).
- [20] L. W. Jin and Y. Su, *Electron. Mater. Lett.* **12**, 371 (2016).
- [21] V. R. Mudinepalli, S. Song, J. Li, and B. S. Murty, *Ceram. Int.* **40**, 1781 (2014).
- [22] J. C. Wang, P. Zheng, R. Q. Yin, L. M. Zheng, J. Du, L. Zheng, J. X. Deng, K. X. Song, and H. B. Qin, *Ceram. Int.* **41**, 14165 (2015).
- [23] H. S. Chen, H. L. Wang, Y. M. Pei, Y. J. Wei, B. Liu, and D. N. Fang, *J. Mech. Phys. Solids* **81**, 75 (2015).
- [24] M. E. Hossain, S. Liu, S. O'Brien, and J. Li, *Appl. Phys. Lett.* **107**, 032904 (2015).
- [25] V. Stepkova, P. Marton, and J. Hlinka, *Phys. Rev. B* **92**, 094106 (2015).
- [26] A. Renuka Balakrishna, J. E. Huber, and I. Münch, *Phys. Rev. B* **93**, 174120 (2016).
- [27] Y. Su, H. Chen, J. J. Li, A. K. Soh, and G. J. Weng, *J. Appl. Phys.* **110**, 084108 (2011).
- [28] W. J. Chen, Y. Zheng, W. M. Xiong, X. Feng, B. Wang, and Y. Wang, *Sci. Rep.* **4**, 5339 (2014).
- [29] R. Xu, J. Zhang, Z. Chen, and L. W. Martin, *Phys. Rev. B* **91**, 144106 (2015).
- [30] Y. Su, N. Liu, and G. J. Weng, *Acta Mater.* **87**, 293 (2015).
- [31] R. Ahluwalia, A. K. Tagantsev, P. Yudin, N. Setter, N. Ng, and D. J. Srolovitz, *Phys. Rev. B* **89**, 174105 (2014).
- [32] Y. Gu, M. Li, A. N. Morozovska, Y. Wang, E. A. Eliseev, V. Gopalan, and L. Q. Chen, *Phys. Rev. B* **89**, 174111 (2014).
- [33] A. Abdollahi and I. Arias, *Acta Mater.* **59**, 4733 (2011).
- [34] Z. A. Wilson, M. J. Borden, and C. M. Landis, *Int. J. Fract.* **183**, 135 (2013).
- [35] J. Wang, S. Q. Shi, L. Q. Chen, Y. L. Li, and T. Y. Zhang, *Acta Mater.* **52**, 749 (2004).
- [36] A. K. Soh, Y. C. Song, and Y. Ni, *J. Am. Ceram. Soc.* **89**, 652 (2006).
- [37] Y. Su and C. M. Landis, *J. Mech. Phys. Solids* **55**, 280 (2007).
- [38] D. Schrade, R. Müller, B. Xu, and D. Gross, *Comput. Methods Appl. Mech. Eng.* **196**, 4365 (2007).
- [39] J. Wang and T. Y. Zhang, *Acta Mater.* **55**, 2465 (2007).
- [40] D. Schrade, R. Müller, D. Gross, and P. Steinmann, *Eur. J. Mech. A: Solids* **49**, 455 (2015).
- [41] W. Chen, Y. Zheng, X. Feng, and B. Wang, *J. Mech. Phys. Solids* **79**, 108 (2015).
- [42] A. F. Devonshire, *Philos. Mag.* **40**, 1040 (1949).
- [43] A. F. Devonshire, *Philos. Mag.* **42**, 1065 (1951).
- [44] A. F. Devonshire, *Adv. Phys.* **3**, 85 (1954).
- [45] W. Zhang and K. Bhattacharya, *Acta Mater.* **53**, 185 (2005).
- [46] Y. Su and G. J. Weng, in *Handbook of Micromechanics and Nanomechanics*, edited by S. Li and X.-L. Gao (Pan Stanford Publishing Ptd. Ltd., Singapore, 2013), p. 73.
- [47] X. Guo, K. Chang, L. Q. Chen, and M. Zhou, *Eng. Fract. Mech.* **96**, 401 (2012).
- [48] F. D. Ma, Y. M. Jin, Y. U. Wang, S. L. Kampe, and S. Dong, *Acta Mater.* **70**, 45 (2014).
- [49] X. Guo, C. Pithan, C. Ohly, C. L. Jia, J. Dornseiffer, F. H. Haegel, and R. Waser, *Appl. Phys. Lett.* **86**, 082110 (2005).

- [50] S. C. Jeon, B. K. Yoon, K. H. Kim, and S. J. L. Kang, *J. Adv. Ceram.* **3**, 76 (2014).
- [51] X. Deng, X. Wang, H. Wen, L. Chen, L. Chen, and L. Li, *Appl. Phys. Lett.* **88**, 252905 (2006).
- [52] L. Curecheriu, S. B. Balmus, M. T. Buscaglia, V. Buscaglia, A. Ianculescu, and L. Mitoseriu, *J. Am. Ceram. Soc.* **95**, 3912 (2012).
- [53] Z. Zhao, V. Buscaglia, M. Viviani, M. T. Buscaglia, L. Mitoseriu, A. Testino, M. Nygren, M. Johnsson, and P. Nanni, *Phys. Rev. B* **70**, 024107 (2004).
- [54] M. Anoufa, J. M. Kiat, I. Kornev, and C. Bogicevic, *Phys. Rev. B* **88**, 144106 (2013).
- [55] M. Rao, H. R. Krishnamurthy, and R. Pandit, *Phys. Rev. B* **42**, 856 (1990).